Optics Letters

Real-time high-speed three-dimensional surface imaging using band-limited illumination profilometry with a CoaXPress interface

Cheng Jiang,[1,†] Patrick Kilcullen,[1,†] Xianglei Liu,[1] Jeremy Gribben,[2] Alan Boate,[2] Tsuneyuki Ozaki,[1] and Jinyang Liang[1,*]

[1]Centre Énergie Matériaux Télécommunications, Institut National de la Recherche Scientifique, 1650 Boulevard Lionel-Boulet, Varennes, Québec J3X1S2, Canada
[2]Ajile Light Industries, 5480 Canotek Road, Unit 6, Ottawa, Ontario K1J9H5, Canada
*Corresponding author: jinyang.liang@emt.inrs.ca

Received 25 September 2019; revised 19 December 2019; accepted 10 January 2020; posted 13 January 2020 (Doc. ID 378939); published 12 February 2020

High-speed three-dimensional (3D) surface imaging by structured-light profilometry is currently driven by numerous applications. However, the limited speeds in fringe pattern projection, image acquisition, and data transmission have strained the existing methods from reaching kilohertz-level acquisition, processing, and display of 3D information during the occurrence of dynamic events (i.e., in real time). To overcome these limitations, we have developed band-limited illumination profilometry (BLIP) with a CoaXPress interface (CI), which enables real-time high-speed 3D surface imaging. We have demonstrated the system's performance by imaging various static and fast-moving 3D objects in real time. We have also applied this system in fluid mechanics by imaging dynamics of a flag, which allowed observation of the wave propagation, gravity-induced phase mismatch, and asymmetric flapping motion. We expect CI-BLIP to find diverse scientific and industrial applications.

https://doi.org/10.1364/OL.378939

Three-dimensional (3D) surface imaging is used in widespread fields. The incessant demands for higher spatial resolution, a larger field of view (FOV), and a higher imaging speed have driven researchers to invent a myriad of 3D surface imaging methods [1–3]. Among them, structured-light profilometry (SLP) has become the mainstream technique [4]. In a typical setup, a projector delivers structured patterns onto an object. The structured patterns, deformed by the object's 3D surface, are captured by a camera. The 3D information is then extracted by analyzing the patterns' deformation with respect to reference phase profiles. Among existing choices of structured patterns in SLP [5], the sinusoidal fringes are most widely used because of their provision of 3D data with both high spatial resolution and high depth accuracy [6] as well as their suitability for high-speed 3D measurements [7]. To generate these fringes, digital micromirror devices (DMDs) are commonly used. Each micromirror on the DMD can be independently tilted to either +12° or −12° from its surface normal to generate binary patterns at up to tens of kilohertz (kHz). By controlling the spatially dependent reflectance via temporal dithering of each micromirror, the DMD can produce grayscale sinusoidal patterns [8]. The DMD-based SLP, flexible in system development and accurate in 3D measurements [9], has been implemented in numerous scientific and industrial applications [10].

Recently, the development of DMD-based SLP has increasingly emphasized high-speed 3D surface imaging in real time (defined as image acquisition, processing, and display during the occurrence of dynamic events [11]). Nonetheless, most existing systems fall short in accomplishing these objectives from the aspects of fringe pattern generation as well as image acquisition and processing. Micromirror-dithering clamps the speed of generating 8-bit grayscale images to around 100 Hz [12], which excludes 3D profilometry of many moving objects [13]. This limitation can be mitigated by using binary defocusing [14], which generates a pseudo-sinusoidal pattern at an unconjugate plane to the DMD by slightly defocusing the projector. However, this method compromises the depth-sensing range [15] and is less flexible when used with binary patterns with different periods. Meanwhile, the DMD's uneven surface [16] could induce image distortion to the defocused sinusoidal patterns at the unconjugate plane, which may decrease measurement accuracy, especially under coherent illumination.

Besides illumination schemes, image acquisition devices and image processing modules in existing SLP systems have limitations. Most high-speed cameras deployed in SLP, despite having ultra-high imaging speeds, are not equipped with a high-speed interface to transfer data on time. This bottleneck also hampers the on-line processing software developed based on graphics processing units (GPUs) [17]. As a result, these systems cannot continuously stream data, limiting their application scope to highly synchronous events.

To overcome these limitations, we developed band-limited illumination profilometry (BLIP) with a CoaXPress Interface (CI). As shown in Fig. 1(a), a continuous-wave laser (671-nm wavelength and 200-mW power) is the light source. After

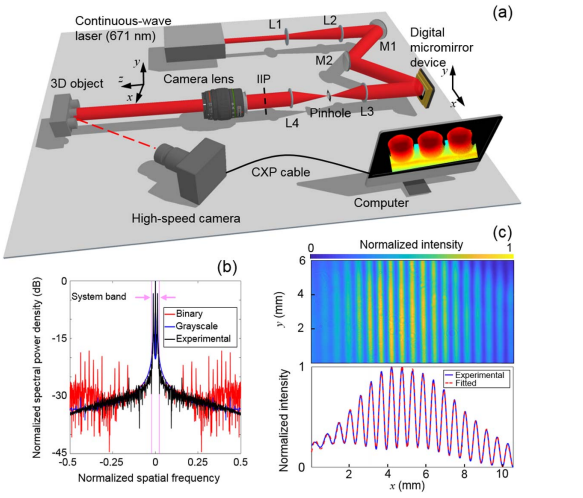

Fig. 1. Operating principle of CI-BLIP. (a) System schematic. Equipment details: continuous-wave laser (MRL-III-671, CNI Lasers), camera lens (AF-P DX NIKKOR, Nikon), digital micromirror device (AJD-4500, Ajile Light Industries), frame grabber (Cyton-CXP, Bitflow), graphics processing unit (GeForce GTX 1060, NVIDIA), high-speed camera (CP70-1HS-M-1900, Optronis), IIP: intermediate image plane, Lenses: L1 (32-990, Edmund Optics), L2 (45-169, Edmund Optics), L3 (63-559, Edmund Optics), L4 (45-895, Edmund Optics), Mirrors: M1 and M2 (BB2-E02, Thorlabs), Pinhole (P150D, Thorlabs). (b) Comparison of the central cross-sections of the spectral power density of the target sinusoidal pattern, the corresponding binary DMD pattern, and experimentally captured image. (c) Top panel: grayscale sinusoidal pattern generated experimentally by band-limited illumination. Bottom panel: the averaged cross-section from the top panel with a fitted result.

expansion and collimation (L1 and L2), the laser beam is directed to a 0.45" DMD at an incident angle of $\sim 24°$ with respect to its surface normal. Binary patterns, loaded onto the DMD, generate sinusoidal fringes at the intermediate image plane by a band-limited 4f imaging system that consists of two lenses (L3 and L4) and one pinhole. Then, a camera lens projects these fringes onto a 3D object with an FOV of 100 mm × 100 mm. The deformed structured images, scattered from the object, are captured by a high-speed CMOS camera, which was synchronized with the DMD at 5 kHz with 512 × 512 pixels in each frame. The captured images are transferred to a computer via a four-channel CoaXPress (CXP) cable connected to a frame grabber. A GPU-based image processing software developed in house is used for on-line 3D image reconstruction.

The real-time, high-speed 3D surface imaging in CI-BLIP is enabled by the following two technical advances. First, we implement band-limited illumination to generate high-quality sinusoidal fringe patterns at 5 kHz. The set of target images contains four grayscale sinusoidal fringe patterns (648-μm period on the DMD) with phase shifts from 0 to $3\pi/2$ with a step of $\pi/2$ as well as one vertical stripe pattern. We first convert each individual grayscale fringe pattern to its corresponding binary DMD pattern using an adaptive error diffusion algorithm [18]. The generated DMD patterns possess blue noise characteristics in the spatial frequency domain [19], manifested by precisely matched imaging content to the corresponding grayscale pattern within the system's bandwidth [Fig. 1(b)]. To filter high-spatial-frequency noise, we place a 150-μm pinhole at the Fourier plane in the 4f imaging system [20]. The resultant beam profiles are high-quality grayscale sinusoidal fringes [Fig. 1(c)], with a root-mean-square error of 4.18% with respect to the target pattern. Compared with the binary defocusing techniques, the band-limited illumination scheme generates accurate sinusoidal patterns at the DMD's conjugate plane, which avoids the depth-dependent blurring effect and image distortion, thus assisting in improving the operating flexibility.

The second technical advance in CI-BLIP lies in the synergy between the high-speed camera interface and the GPU-based processing, which allows real-time high-speed 3D image reconstruction. We first calibrate CI-BLIP for 3D coordinate determination [21]. In data processing, the CXP cable, with a bandwidth of 25 Gbps, enables continuous streaming of fringe images to the computer during image acquisition at 5 kHz. These images are stored into RAM via direct memory access operations independent from the CPU. After determining the vertical stripe pattern, we process the calibration frame and four fringe patterns in GPU, beginning with the parallelized extraction of the wrapped phase and quality map information. We then carry out phase unwrapping via our GPU accelerated implementation of a two-dimensional (2D) weighted phase unwrapping algorithm [22], which uses the quality map information to guide the unwrapping procedure against errors induced by noise. The selected algorithm relies on the independent manipulation of points using 2D discrete cosine transformation [23]. The absolute phase is then computed in parallel by adding a constant determined from the vertical stripe pattern [24]. Finally, we recover coordinate information from the absolute phase map from each pixel via matrix inversion. The resulted software enables real-time full-field 3D surface information reconstruction at 60 Hz. It also allows off-line 3D imaging and real-time 3D position tracking of a single user-selectable point at 1 kHz.

To quantify the depth resolution of CI-BLIP, we imaged two stacked planar surfaces offset by $\sim 5°$ [Fig. 2(a)]. In this configuration, the depth difference between the two surfaces along the x axis increased monotonously, starting from a negative maximum at the right edge, to zero at the center, and reaching a positive maximum at the left edge. The reconstructed image of the 3D object [Fig. 2(b)] allowed analyzing cross-sections of depth at different x positions. We calculated the depth difference (denoted by Δz) of the two surfaces, which closely agrees to the ground truth [Fig. 2(c)]. In addition, standard deviations of the measured depths were used as the system's noise level. The depth resolution was defined as when Δz equals to two times of the system's noise level. CI-BLIP's depth resolution was 0.15 mm.

To examine the feasibility of CI-BLIP, we imaged various static 3D objects. First, we measured three interlocking brick toys, whose studs had the heights of 23 mm, 15 mm, and 3 mm,

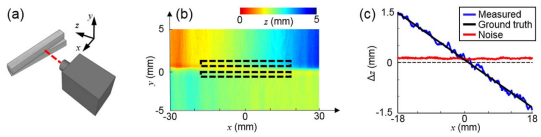

Fig. 2. Quantification of CI-BLIP's depth resolution. (a) Experimental setup. (b) Reconstructed image of the planar surfaces. Black dashed boxes represent the selected regions for analysis. (c) Measured depth difference between the planar surfaces.

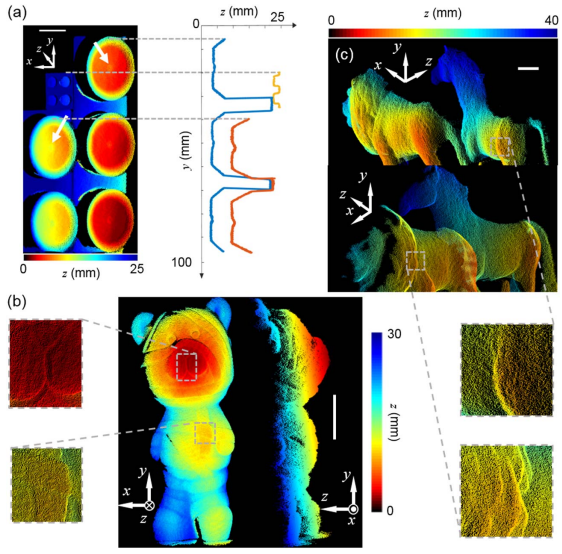

Fig. 3. CI-BLIP of static 3D objects. (a) Reconstructed image of interlocking brick toys (left) and depth profiles of selected centerlines (right). (b) and (c) Reconstruction results of a bear toy (b) as well as a lion toy and a horse toy (c) with different perspective angles and close-up views. Scalar bar: 10 mm.

respectively. Reconstructed results and selected centerlines are plotted in Fig. 3(a). The structure information of these brick toys is accurately recovered, manifested by the identification of shallow dents with depths of ∼ 1 mm at the centers of the studs [see white arrows in Fig. 3(a)]. We also conducted proof-of-concept experiments on single and multiple animal toys [Figs. 3(b) and 3(c)]. In both cases, the depth information is shown in two perspective images and the detailed surface structures are illustrated by close-up views.

To verify real-time high-speed 3D surface profilometry, we used CI-BLIP to image an operating electric fan that rotated at 300 rounds per minute. The fan has seven blades, each having a tilt angle of ∼ 30°. Figure 4(a) shows the front view of the off-line reconstructed 3D images at four time points (full evolution is shown in Visualization 1). Along with a representative side view [Fig. 4(b)], these results allow us to identify detailed 3D shapes of the base, center hub, side cover, blades, and the bars underneath the blades. CI-BLIP enabled tracking the evolution of depth over the entire FOV. As an example, Fig. 4(c) gives line profiles along the radial direction [marked by the black solid line in the first panel of Fig. 4(a)] over time. The blade quickly swept through the radial profile in 10 ms, resulting in a maximum change in depth of 6 mm. To further analyze details in depth dynamics, in Fig. 4(d), we plot the depth profiles of three points on the line—one on the central hub (p_A), two along a blade (p_B and p_C). The depth profiles of p_A to p_C clearly illustrate the linear relationship between the displacements of the fan blades with different radii at a constant angular speed of ∼ 30 rad/s, well agreeing with preset conditions. Finally, Visualization 2 shows real-time, high-speed imaging of a swinging pendulum and a bear statue using CI-BLIP. Selected results from the real-time reconstruction of this scene were displayed at 60 Hz. The demonstration also showed real-time 1-kHz 3D position tracking of a user-selectable single point.

To highlight the broad utility of CI-BLIP, we used it to image flapping dynamics of a flag. In our experiment, a flag with a

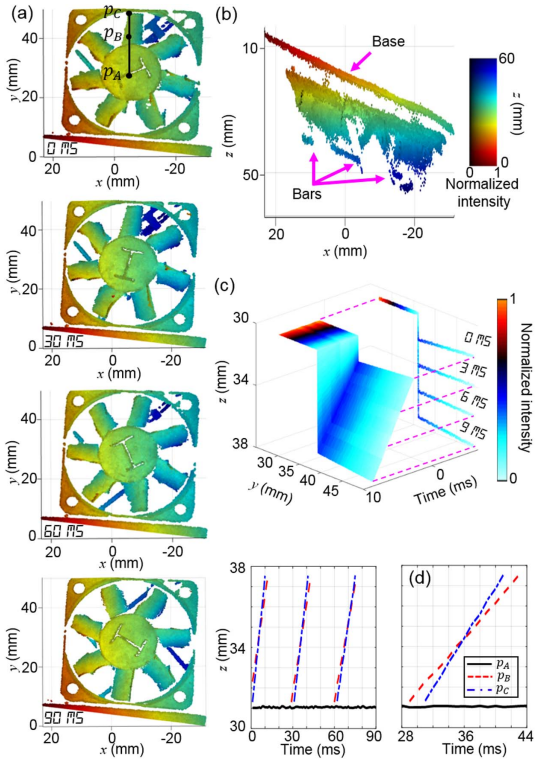

Fig. 4. CI-BLIP of a high-speed operating fan. (a) Front view of reconstructed 3D images at four different time points. (b) Side view of the reconstructed 3D image at 60 ms. (c) Depth line profiles along the radial direction over time. (d) Depth dynamics of the three selected points marked in the first panel in (a).

maple leaf pattern (80 mm × 50 mm in size) was mounted on a pole. An air blower generated strong wind interacting with the flag. Figure 5(a) depicts four representative 3D images of the instantaneous poses of the flapping flag from two perspective views (see the full sequence in Visualization 3), showing a wave traveling toward the edge at approximately 2 m/s. Displayed in Fig. 5(b), we analyzed time histories of the streamwise (x axis), spanwise (y axis), and transverse (z axis) displacements of three selected points [marked as p_A, p_B, and p_C in Fig. 5(a)]: p_A is at the mid- point in the y axis; p_B and p_C have the same x coordinate. The displacements of p_A have the smallest amplitudes in all three directions, showing a less intense flapping motion in the part closer to the pole.

Moreover, the streamwise and transverse displacements of p_B and p_C show an apparent phase difference, which is probably attributed to the gravity-induced sagging effect. Furthermore, the phase relation between the spanwise and transverse displacements of p_C [Fig. 5(c)] show an elliptical shape in both experimental and fitted results, demonstrating that the flapping motion is dominated by single-frequency sinusoidal waves. Finally, the depth curves of the flag's centerline in all reconstructed images [Fig. 5(d)] show asymmetric flapping motion toward the $-z$ direction, which indicates the uneven forces to the flag surface and a relatively high degree of turbulent flow.

We have developed CI-BLIP that integrates band-limited illumination, CoaXPress-interfaced high-speed image acquisition, and GPU-based image reconstruction. This high-speed SLP system has enabled, for the first time, real-time 3D position tracking of a single user-selectable point at 1 kHz. The

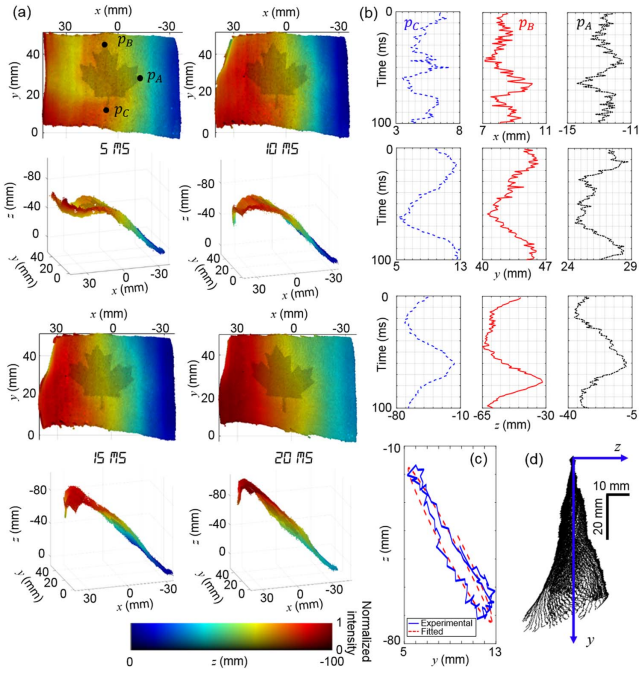

Fig. 5. CI-BLIP of a flapping flag. (a) Two perspective views of reconstructed 3D images of a flapping flag at different times. (b) Evolution of 3D positions of the three selected points marked in the first panel in (a). (c) Phase relation of the y-z positions of p_C and the fitted result. (d) Superimposed centerlines of the flag over time. Note: The depth of the pole is defined to zero in the z axis.

major specifications could be further improved by using a high-power laser, a faster camera interface [25], and advanced phase unwrapping algorithms [26].

CI-BLIP will likely open new avenues for diverse applications, including *in-situ* industrial inspection [27], dynamic biometric analysis [28], and acoustic vibrometry [29]. In particular, we expect it to immediately benefit studies of flag-fluid interactions. The mechanisms that govern these phenomena have generated scientific interests in diverse studies [30]. Due to the flag's complex geometries and freely moving boundaries [31], study of the gravity-induced impact in its interaction with fluid remains a challenge. Thus far, although many simulation works have been carried out to investigate the relation between gravity and the flag's stability with different flow air conditions [32], experimental visualization of real-time flag movement has not kept up. A limited number of previous experiments were conducted using low flow speeds to avoid the complication induced by the flag dragging its support [33]. In addition, rigid flags were used in these experiments, which, however, restricted the analysis of fluid dynamics in 2D. In contrast, CI-BLIP has empowered the high-speed 3D analysis of the wave propagation, gravity-induced phase mismatch, and asymmetric flapping motion of a non-rigid flag. These experiments may pave the way for potential future studies of high-speed nonlinear flapping dynamics [34]. CI-BLIP's ability to continuously stream acquired data could also contribute to imaging unpredicted or non-repeatable flow dynamics.

Funding. Natural Sciences and Engineering Research Council of Canada (RGPIN-2017-05959, 158249-17, RGPAS-507845-2017); Canada Foundation for Innovation (37146); Fonds de Recherche du Québec - Nature et Technologies (2019-NC-252960); Fonds de Recherche du Québec - Santé (267406, 280229).

Disclosures. The authors declare no conflicts of interest.

†These authors contribute equally to this work.

REFERENCES

1. M. Gosta and M. Grgic, in *Proceedings ELMAR* (IEEE, 2010), p. 57.
2. M. Hansard, S. Lee, O. Choi, and R. P. Horaud, *Time-of-Flight Cameras: Principles, Methods and Applications* (Springer, 2012).
3. S. Zhang, Opt. Laser Eng. **48**, 149 (2010).
4. S. Zhang, Opt. Laser Eng. **107**, 28 (2018).
5. J. Geng, Adv. Opt. Photon. **3**, 128 (2011).
6. C. Zuo, S. Feng, L. Huang, T. Tao, W. Yin, and Q. Chen, Opt. Laser Eng. **109**, 23 (2018).
7. S. S. Gorthi and P. Rastogi, Opt. Laser Eng. **48**, 133 (2010).
8. L. J. Hornbeck, Proc. SPIE **3013**, 27 (1997).
9. X. Su and Q. Zhang, Opt. Laser Eng. **48**, 191 (2010).
10. B. Li and S. Zhang, Meas. Sci. Technol. **29**, 045402 (2018).
11. S. Van der Jeught and J. J. Dirckx, Opt. Laser Eng. **87**, 18 (2016).
12. S. Zhang, Opt. Laser Eng. **106**, 119 (2018).
13. C. Zuo, T. Tao, S. Feng, L. Huang, A. Asundi, and Q. Chen, Opt. Laser Eng. **102**, 70 (2018).
14. B. Li, Y. Wang, J. Dai, W. Lohry, and S. Zhang, Opt. Laser Eng. **54**, 236 (2014).
15. S. Lei and S. Zhang, Opt. Lett. **34**, 3080 (2009).
16. V. Parthiban, R. N. Kohn, Jr., J. Liang, and M. F. Becker, Proc. SPIE **9761**, 97610M (2016).
17. T. D. Han and T. S. Abdelrahman, IEEE Trans. Parallel Distrib. Syst. **22**, 78 (2010).
18. K. L. Chung, S. C. Pei, Y. L. Pan, W. L. Hsu, Y. H. Huang, W. N. Yang, and C. H. Chen, Exp. Syst. Appl. **38**, 1591 (2011).
19. J. Liang, S.-Y. Wu, R. N. Kohn, M. F. Becker, and D. J. Heinzen, Opt. Eng. **51**, 108201 (2012).
20. J. Liang, M. F. Becker, R. N. Kohn, and D. J. Heinzen, J. Micro/Nanolithogr., MEMS, MOEMS **11**, 023002 (2012).
21. S. Zhang and P. S. Huang, Opt. Eng. **45**, 083601 (2006).
22. D. C. Ghiglia and L. A. Romero, J. Opt. Soc. Am. A **11**, 107 (1994).
23. https://developer.nvidia.com/cufft.
24. J. Makhoul, IEEE Trans. Acoust. Signal Process. **28**, 27 (1980).
25. X. Liu, J. Liu, C. Jiang, F. Vetrone, and J. Liang, Opt. Lett. **44**, 1387 (2019).
26. J.-S. Hyun and S. Zhang, Appl. Opt. **55**, 4395 (2016).
27. K. Zhong, Z. Li, X. Zhou, Y. Li, Y. Shi, and C. Wang, Int. J. Adv. Man. Tech. **76**, 1563 (2015).
28. A. Chatterjee, P. Singh, V. Bhatia, and S. Prakash, Opt. Laser Technol. **112**, 368 (2019).
29. M. Akutsu, Y. Oikawa, and Y. Yamasaki, in *ASA Proceedings of Meetings on Acoustics ICA* (ASA, 2013), p. 055019.
30. S. Banerjee, B. S. Connell, and D. K. Yue, J. Fluid Mech. **783**, 103 (2015).
31. W.-X. Huang and H. J. Sung, J. Fluid Mech. **653**, 301 (2010).
32. S. Alben and M. J. Shelley, Phys. Rev. Lett. **100**, 074301 (2008).
33. J. Zhang, S. Childress, A. Libchaber, and M. Shelley, Nature **408**, 835 (2000).
34. M. Argentina and L. Mahadevan, Proc. Natl. Acad. Sci. USA **102**, 1829 (2005).